Gemini NIFS survey of feeding and feedback processes in nearby Active Galaxies: II -The sample and surface mass density profiles

R. A. Riffel[1]*, T. Storchi-Bergamann[2], R. Riffel[2], R. Davies[3], M. Bianchin[1],
M. R. Diniz[1], A. J. Schönell[2,4], L. Burtscher[5], M. Crenshaw[6], T. C. Fischer[7],
L. G. Dahmer-Hahn[2], N. Z. Dametto[2], D. Rosario[8]

[1] *Departamento de Física, CCNE, Universidade Federal de Santa Maria, 97105-900, Santa Maria, RS, Brazil*
[2] *Departamento de Astronomia, IF, Universidade Federal do Rio Grande do Sul, CP 15051, 91501-970, Porto Alegre, RS, Brazil*
[3] *Max-Planck-Institut für extraterrestrische Physik, Postfach 1312, D-85741, Garching, Germany*
[4] *Instituto Federal de Educação, Ciência e Tecnologia Farroupilha, BR287, km 360, Estrada do Chapadão, 97760-000, Jaguari - RS, Brazil*
[5] *Leiden Observatory, Leiden University, PO Box 9513, 2300 RA Leiden, The Netherlands*
[6] *Department of Physics and Astronomy, Georgia State University, Astronomy Offices, 25 Park Place, Suite 605, Atlanta, GA 30303, USA*
[7] *Astrophysics Science Division, Goddard Space Flight Center, Code 665, Greenbelt, MD 20771, USA.*
[8] *Department of Physics, Durham University, South Road, Durham DH1 3LE, UK*

ABSTRACT

We present and characterize a sample of 20 nearby Seyfert galaxies selected for having BAT 14–195 keV luminosities $L_X \geq 10^{41.5}$ ergs s^{-1}, redshift $z \leq 0.015$, being accessible for observations with the Gemini Near-Infrared Field Spectrograph (NIFS) and showing extended [OIII]λ5007 emission. Our goal is to study Active Galactic Nuclei (AGN) feeding and feedback processes from near-infrared integral-field spectra, that include both ionized (H II) and hot molecular (H$_2$) emission. This sample is complemented by other 9 Seyfert galaxies previously observed with NIFS. We show that the host galaxy properties (absolute magnitudes M_B, M_H, central stellar velocity dispersion and axial ratio) show a similar distribution to those of the 69 BAT AGN. For the 20 galaxies already observed, we present surface mass density (Σ) profiles for H II and H$_2$ in their inner $\sim$500 pc, showing that H II emission presents a steeper radial gradient than H$_2$. This can be attributed to the different excitation mechanisms: ionization by AGN radiation for H II and heating by X-rays for H$_2$. The mean surface mass densities are in the range $(0.2 \leq \Sigma_{HII} \leq 35.9)$ M$_\odot$ pc^{-2}, and $(0.2 \leq \Sigma_{H2} \leq 13.9) \times 10^{-3}$ M$_\odot$ pc^{-2}, while the ratios between the H II and H$_2$ masses range between $\sim$200 to 8000. The sample presented here will be used in future papers to map AGN gas excitation and kinematics, providing a census of the mass inflow and outflow rates and power as well as their relation with the AGN luminosity.

Key words: galaxies: active – galaxies: nuclei – infrared: galaxies

1 INTRODUCTION

The co-evolution of Active Galactic Nuclei (AGN) and galaxies is now an accepted paradigm that permeates recent reviews (Kormendy & Ho 2013; Heckman & Best 2014). But the conclusions put forth in these reviews are mostly based on surveys of integrated galaxy properties, and the feeding and feedback processes that lead to the co-evolution

have been implemented in models in a simplistic way Somerville et al. (2008); Springel et al. (2005); Croton et al. (2006). This is due to the lack of observational constraints from spatially resolved studies. Physical motivated models Hopkins & Quataert (2010) show that the relevant feeding processes occur within the inner kiloparsec, that can only be resolved in nearby galaxies. The large quantities of dust in the inner kiloparsec of AGN, estimated to range from 10^5 to 10^7 M$_\odot$ (Simões Lopes et al. 2007; Martini, Dicken & Storchi-Bergmann 2013; Audibert et al.

* E-mail: rogemar@ufsm.br

2017) and the associated large content of molecular gas (10^7 to 10^9 M$_\odot$) points to the importance of looking for signatures of the feeding in the molecular gas within the nuclear region. Recently it has also been argued that the feedback in the form of massive outflows is also dominated by molecular gas (Sakamoto et al. 2010; Aalto et al. 2012; Veilleux et al. 2013), at least in LIRGS or ULIRGS (Ultra Luminous Infrared Galaxies).

The co-evolution scenario, and the feeding of gas to the inner kiloparsec of galaxies when they are in the active phase, implies that the galaxy bulge grows in consonance with the SMBH. Since the early studies of Terlevich and collaborators (e.g. Terlevich et al. 1990), it has been argued that the excess blue light and dilution of the absorption features of the nuclear spectra of active galaxies was due to young stars. Subsequent long-slit studies (Storchi-Bergmann et al. 2000; Cid Fernandes et al. 2004; Davies et al. 2007; Kauffmann & Heckman 2009) have found an excess contribution of young to intermediate age stars to the stellar population in the inner kiloparsec of active galaxies when compared to non-active ones. This result has led to the proposition of an evolutionary scenario (Storchi-Bergmann et al. 2001; Davies et al. 2007; Hopkins 2012), in which the gas inflow to the nuclear region first triggers star formation in the circumnuclear region, and is then followed by the ignition of the nuclear activity.

Observational constraints for the feeding and feedback processes can be obtained via spatially resolved studies of nearby active galaxies using integral field spectroscopy (IFS). The radiation from the AGN heats and ionizes the surrounding gas in the galaxy up to hundreds of pc (and even kpc) scales. The heating excites rotational and vibrational states of the H$_2$ molecule that then emits in the near-IR, and the AGN radiation ionizes the gas that, in turn, emits permitted and forbidden lines that can be used to probe the ionized gas kinematics and excitation. Emission from both the molecular and ionized gas phases can be observed in the near-IR domain, where the effects of dust extinction is minimized. In the near-infrared, IFS at 10 meter class telescopes has been used to probe the feeding and feedback processes in nearby active galaxies, by mapping and modeling the molecular and ionized gas kinematics in the inner kiloparsec of active galaxies – on 10–100 pc scales – leading to insights on both the feeding and feedback mechanisms. For high signal-to-noise ratio in the continuum, the stellar kinematics as well as the age distribution of the stellar population have also been mapped. So far, these studies show that (i) Emission from molecular (H$_2$) and ionized gases present distinct flux distributions and kinematics. The H$_2$ emission is distributed all around the nucleus, seems to be located in the plane of the galaxy, shows low velocity dispersion ($<100 \, \mathrm{km \, s^{-1}}$) and is dominated by rotational motion. In few cases, a very steep rotation curve is observed, suggesting the presence of compact molecular disks Riffel & Storchi-Bergmann (2011a); Schönell et al. (2014); Hicks et al. (2013); Mazzalay et al. (2014). In a number of cases, streaming motions towards the central regions were mapped along nuclear spiral arms with estimated inflow rates in total molecular gas ranging from a few tenths to a few solar masses per year (Riffel et al. 2008; Riffel, Storchi-Bergmann & Winge 2013; Davies et al. 2009; Müller-Sánchez et al. 2009; Diniz et al.

2015). (ii) The ionized gas emission is more collimated and shows higher velocity dispersion ($>100 \, \mathrm{km \, s^{-1}}$) than the molecular gas, seems to extend to high latitudes and its kinematics comprises both rotation and outflow (e.g. Riffel et al. 2006; Riffel, Storchi-Bergmann & Nagar 2010; Müller Sánchez et al. 2011; Riffel, Storchi-Bergmann & Winge 2013; Barbosa et al. 2014; Storchi-Bergmann et al. 2010). (iii) Only for a few cases, the study of stellar population was done using near-IR IFS. These works show the presence of young to intermediate age ($\sim 10^8$ yr) stars, usually in $\sim 100 \, \mathrm{pc}$ rings (e.g. Riffel et al. 2010, 2011c; Storchi-Bergmann et al. 2012), that correlate with rings of low velocity dispersion. This correlation has been interpreted as being a signature of the co-evolution of the bulge and SMBH: as the estimated mass inflow rates are ~ 3 orders of magnitude larger than the accretion rate to the AGN, most of the molecular gas that is accumulated in the nuclear regions of AGNs is forming new stars in the inner few hundred parsecs of the galaxy, leading to the growth of the bulge.

Most of the results summarized above were obtained by studying individual galaxies, selected using distinct criteria, and a study of a well-defined, comprehensive sample is of fundamental importance to understand the relation among AGN feeding, feedback and galaxy evolution (e.g. Davies et al. 2017). In the present work, we describe a sample of nearby active galaxies that are being observed with the Gemini Near-Infrared Integral Field Spectrograph (NIFS). Our aim with these observations is to study the details of the inner few hundreds of parsecs of AGNs and better constrain the feeding and feedback processes. This is the second paper of a series in which we will be mapping the gas excitation and kinematics, as well as the stellar population characteristics and kinematics. In the first paper (Riffel et al. 2017), we have presented and discussed stellar kinematics measurements for 16 galaxies of the sample and in forthcoming papers we will analyse the emission-line flux distributions, gas kinematics and map the stellar populations. This paper is organized as follows: Section 2 describes the selection criteria of the sample, the instrument configuration, observations, data reduction and compare nuclear and large scale properties of the galaxies. In section 3 we present and discuss measurements of the molecular and ionized gas masses and surface densities for the galaxies already observed and Section 4 discusses the implications of the derived amount of gas to the AGN feeding process and star formation. Finally, section 5 presents the conclusions of this work.

2   DEFINITION OF A SAMPLE AND OBSERVATIONS

2.1   The sample

In order to select out an AGN sample, we used the Swift-BAT 60-month catalogue (Ajello et al. 2012), and selected nearby galaxies with 14–195 keV luminosities $L_X \geq 10^{41.5}$ ergs s^{-1} and redshift $z \leq 0.015$. The hard (14–195 keV) band of the Swift-BAT survey measures direct emission from the AGN rather than scattered or re-processed emission, and is much less sensitive to obscuration in the line-of-sight than

soft X-ray or optical wavelengths, allowing a selection based only on the AGN properties. Davies et al. (2015) describe a southern hemisphere sample selected in a similar way and discuss its rationale for studying AGN feeding and feedback processes (see also, Davies et al. 2017). Although their sample includes brighter and closer galaxies then ours, being composed by galaxies with $\log L_X = 42.4 - 43.7$ and $z < 0.01$.

As additional criteria, the object must be accessible for Gemini NIFS ($-30° < \delta < 73°$) and its nucleus being bright/pointy enough to guide the observations or with natural guide stars available in the field. Finally, we only have included in the sample galaxies already previously observed in the optical and with extended [O III]λ5007 emission available in the literature. We have used this constraint in order to ensure that we will have extended gas emission to allow spatially resolve its kinematics and look for possible inflows and outflows. From our previous experience, a galaxy that shows extended [O III] emission will also have a similarly extended [Fe II] or Paβ emission. Table 1 presents the resulting sample, which is composed of 20 galaxies. In addition, we included 9 galaxies observed with NIFS by our group in previous works (shown below the horizontal line in Table 1). These aditional galaxies may be used as a complementary sample in forthcoming works.

Figure 1 shows a plot of L_X vs. z for all Swift BAT AGN with $z \leq 0.05$ and accessible to Gemini North ($-30^0 < \delta < 73^0$).Green diamonds show the galaxies accessible to Gemini North that satisfy the following criteria: $L_X \geq 10^{41.5}$ ergs s^{-1} and $z \leq 0.015$, while the red squares show our main sample (objects that satisfy all the requirements above). The cyan $\times$ symbols show the objects of the complementary sample detected in the Swift-BAT 60-month catalogue. The red dotted line shows the detection limit of the Swift 60-month catalogue and the vertical and horizontal lines show the L_X and z cuts used to define our sample, respectively.

2.2 Characterization of the sample

It is well known that hard X-ray emission is a good tracer of nuclear activity in galaxies, and thus a X-ray selected sample is representative of the population of AGN within the limited volume. However, besides the limits in X-ray luminosity and redshift, we included a constraint based on the detection of [O III]λ5007 emission line in order to increase the rate of detection of extended emission in near-IR lines, necessary to map the gas kinematics and flux distributions. In order to test if this additional criteria produces any bias on our sample, as compared to objects selected only on the basis of their X-ray emission, we compare the distribution of physical properties of the nucleus and host galaxies of the BAT sample (composed of galaxies with $L_X \geq 10^{41.5}$ ergs s^{-1} and redshift $z \leq 0.015$) with the distributions of our main and complementary samples.

The total number of galaxies in the 60 month BAT catalogue that follows the constraints above is 69 galaxies (hereafter we will call this sample as the "restricted BAT sample"), while our main sample is composed of 20 objects, as shown in Table 1. In the left panel of Figure 2 we present a histogram for the distribution of L_X of our main sample in bins of $\log L_X = 0.3$ crosshatched histogram, overlaid on the histogram for the restricted BAT sample, which is shown in gray. As can be observed in this plot, both sam-
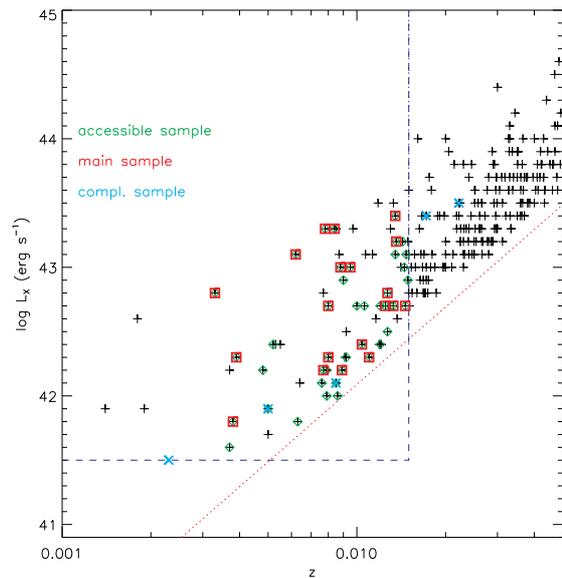
Figure 1. Plot of L_X vs. z for the galaxies of our sample. Black crosses show all objects (257) with $\log L_X > 41.5$ at the Swift BAT 60-month catalogue, green diamonds represent objects (43) accessible by NIFS ($-30° < \delta < 73°$), red squares represent our main sample (20) and cyan crosses are objects from our complementary sample detected in Swift BAT. All points at $z < 0.015$ make up what we call "the restricted BAT sample", composed by 69 galaxies. The red dotted line shows the detection limit of Swift and the dashed lines show the limits in L_X and z used the NIFS sample ($L_X \geq 10^{41.5}$ ergs s^{-1} and $z \leq 0.015$).

ples show a very similar distribution with mean luminosities of $< \log L_X >= 42.6 \pm 0.1$ erg s^{-1} and $< \log L_X >= 42.7 \pm 0.1$ erg s^{-1} for the BAT and our main sample, respectively. We performed a Kolmogorov-Smirnov (K-S) statistic test to estimate the K-S confidence index (KS) and the probability of the two distributions being drawn from the same distribution (P). The resulting parameters are $KS = 0.143$ and $P = 0.886$, indicating that both restricted BAT and main samples have a probability of $\sim$89 % of being originated from the same distribution. Thus, the inclusion of the additional selection criteria of having extended [O III] emission already published and being observable with NIFS does not change significantly the distribution of the sample in terms of X-ray luminosities and our main sample can be considered a representative sample of nearby AGNs within adopted constrains in X-ray luminosity and redshift. It is already well known that a close correlation between the [O III] and hard X-ray luminosities is observed for AGNs (e.g. Lamperti et al. 2017) and that a better correlation is found if the sample is selected based on the X-ray luminosity than if it is drawn from [O III] luminosity (Heckman & Best 2014). As our sample is based on the X-ray luminosity, the similarity in the X-ray distribution is both samples is expected.

Five galaxies of the complementary sample have X-ray luminosities available in the 60 month BAT catalogue. Including these sources, the distribution of galaxies shows an extension to lower X-ray luminosities as seen in the central panel of Fig. 2, filling the low-luminosity "gap" seen in the main sample, as only one galaxy of the complementary sam-

Table 1. The sample. (1) Galaxy name; (2) Redshift; (3) Morphological classification; (4) Nuclear Activity (from quoted in NED), (5) Swift 14-195 keV luminosity, (6) [O III]λ5007 luminosity in units of ergs s^{-1}, (7) reference for the [O III] luminosity. Table 2 list the galaxies already observed.

(1) Galaxy	(2) z	(3) Hubble Type	(4) Nuc. Act.	(5) $\log(L_X)$	(6) $\log(L_{OIII})$	(7) Ref.
Main sample						
NGC788	0.014	SA0/a?(s)	Sy2	43.20	41.06	a
NGC1068	0.004	(R)SA(rs)b	Sy2	41.80	41.53	b
NGC1125	0.011	(R')SB0/a?(r)	Sy2	42.30	39.69	c
NGC1194	0.013	SA0$^+$?	Sy1	42.70	39.60	b
NGC2110	0.008	SAB0$^-$	Sy2	43.30	40.64	a
Mrk3	0.014	S0?	Sy2	43.40	41.83	b
NGC2992	0.008	Sa pec	Sy2	42.20	41.42	a
NGC3035	0.015	SB(rs)bc	Sy1	42.70	39.83	c
NGC3081	0.008	(R)SAB0/a(r)	Sy2	42.70	41.58	a
NGC3227	0.004	SAB(s)a pec	Sy1.5	42.30	40.84	a
NGC3393	0.013	(R')SB(rs)a?	Sy2	42.70	41.58	b
NGC3516	0.009	(R)SB0^0?(s)	Sy1.5	43.00	41.02	b
NGC3786	0.009	SAB(rs)a pec	Sy1.8	42.20	40.59	a
NGC4151	0.003	(R')SAB(rs)ab?	Sy1.5	42.80	42.19	a
NGC4235	0.008	SA(s)a edge-on	Sy1	42.30	39.31	a
Mrk766	0.013	(R')SB(s)a?	Sy1.5	42.80	41.10	b
NGC4388	0.008	SA(s)b? edge-on	Sy2	43.30	41.26	b
NGC4939	0.010	SA(s)bc	Sy1	42.40	40.64	c
NGC5506	0.006	Sa pec edge-on	Sy1.9	43.10	40.97	a
NGC5728	0.009	SAB(r)a?	Sy2	43.00	41.47	a
Complementary Sample						
NGC1052	0.005	E4	Sy2	41.90	–	–
NGC4051	0.002	SAB(rs)bc	Sy1	41.50	–	–
NGC5548	0.017	(R')SA0/a(s)	Sy1	43.40	41.37	b
NGC5899	0.009	SAB(rs)c	Sy2	42.10	–	–
NGC5929	0.008	Sab? pec	Sy2	–	–	–
Mrk79	0.022	SBb	Sy1	43.50	41.58	b
Mrk607	0.009	Sa? edge-on	Sy2	–	–	–
Mrk1066	0.012	(R)SB0$^+$(s)	Sy2	–	–	–
Mrk1157	0.015	(R')SB0/a	Sy2	–	–	–

References: a: Wittle (1992), b: Schmitt et al. (2003), c: Gu et al. (2006); d: Noguchi et al. (2010); e: Zhu et al. (2011).
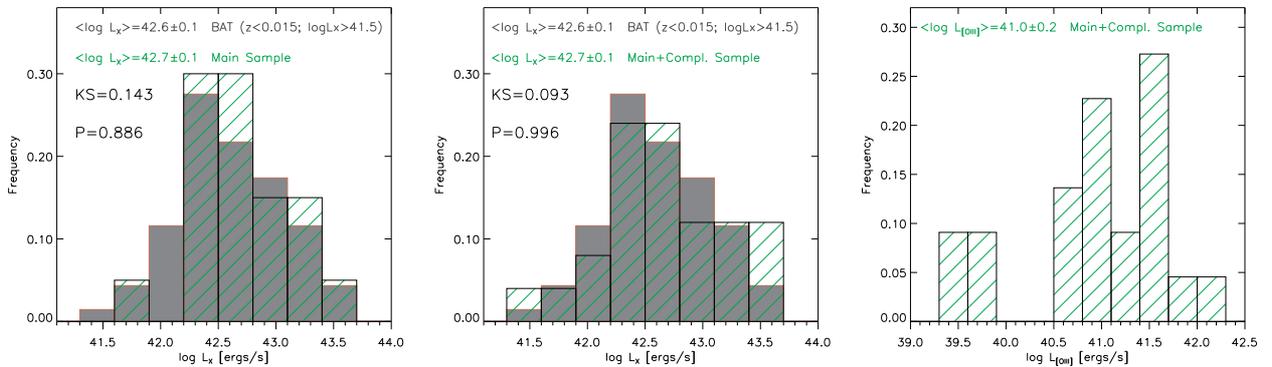
Figure 2. Histograms for the distribution of X-ray and [O III]λ5007 luminosities of the galaxies of our sample. The left panel shows the distribution of $\log L_X$ of all galaxies with $L_X \geq 10^{41.5}$ ergs s^{-1} and $z \leq 0.015$ from the 60 month BAT catalogue (the "restricted BAT" sample) in gray, with the distribution of our main sample overploted and crosshatched green histogram. In the central panel, the complementary sample is included and the right panel shows the distribution of the [O III]λ5007 luminosities for our sample, including the two objects from the complementary sample with [O III] luminosities available. All histograms were constructed using a bin of $\log L_X = 0.3$ ergs s^{-1} and the mean values for each distribution are shown at the top of each panel. The results for the K-S statistical test (*KS* and *P*) are shown are shown for the first two panels.
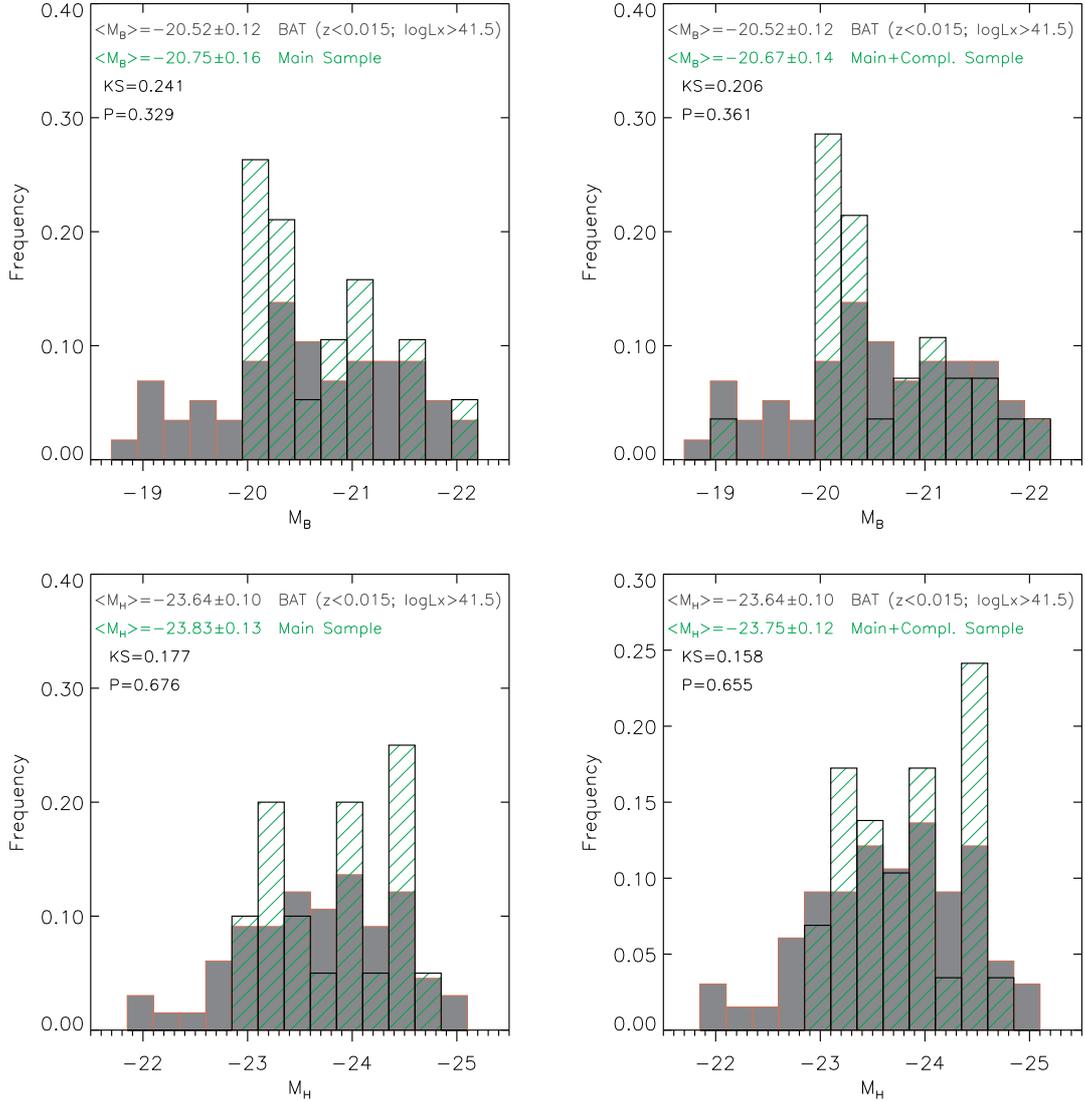
Figure 3. Distribution of B (top) and H (bottom) band absolute magnitudes for the galaxies of the main sample (left) and main+complementary sample (right) in bins of 0.25 mag. The distribution of the BAT sample is shown as the gray histogram. The results for the K-S statistical test (*KS* and *P*) are shown in each panel.

ple shows $\log L_X > 42.3$. However, the averaged luminosity does not change, as the complementary sample includes also two high luminosity objects (NGC 5548 and Mrk 79). The K-S test indicates that the inclusion of these sources makes the sample even more similar to the restricted BAT sample, with almost 100 % of probability of both samples follow the same distribution in L_X. Besides the 20 galaxies of our main sample, [O III]λ 5007 luminosities are available for two galaxies of the complementary sample. Our combined (main + complementary) sample shows [O III]λ 5007 luminosities in the range $L_{[OIII]} = (0.2 - 155) \times 10^{40}$ erg s^{-1}, with a mean value of $< \log L_{[OIII]} > = 41.0 \pm 0.2$ erg s^{-1}.

We compiled physical properties of the host galaxies from the Hyperleda database [1] (Makarov et al. 2014) and

NED[2]. In figures 3 and 4 we present histograms for the absolute B (top panels of Fig. 3) and H magnitudes (bottom panels of Fig. 3), the nuclear stellar velocity dispersion (top panels of Fig. 4) and axial ratio (bottom panels of Fig. 4). Both magnitudes correspond to apertures that include the the total emission of the host galaxy. The left panels of these figures show the distribution of these properties for the main sample, while the right panels show the same properties for the combined sample. As in Fig. 2 the restricted BAT sample is shown as the gray histogram.

The B absolute magnitude M_B was obtained from the Hyperleda database, and is available for 58 objects from the restricted BAT sample and for 28 galaxies of our sample, the only exception being NGC 3035. The mean value of M_B for
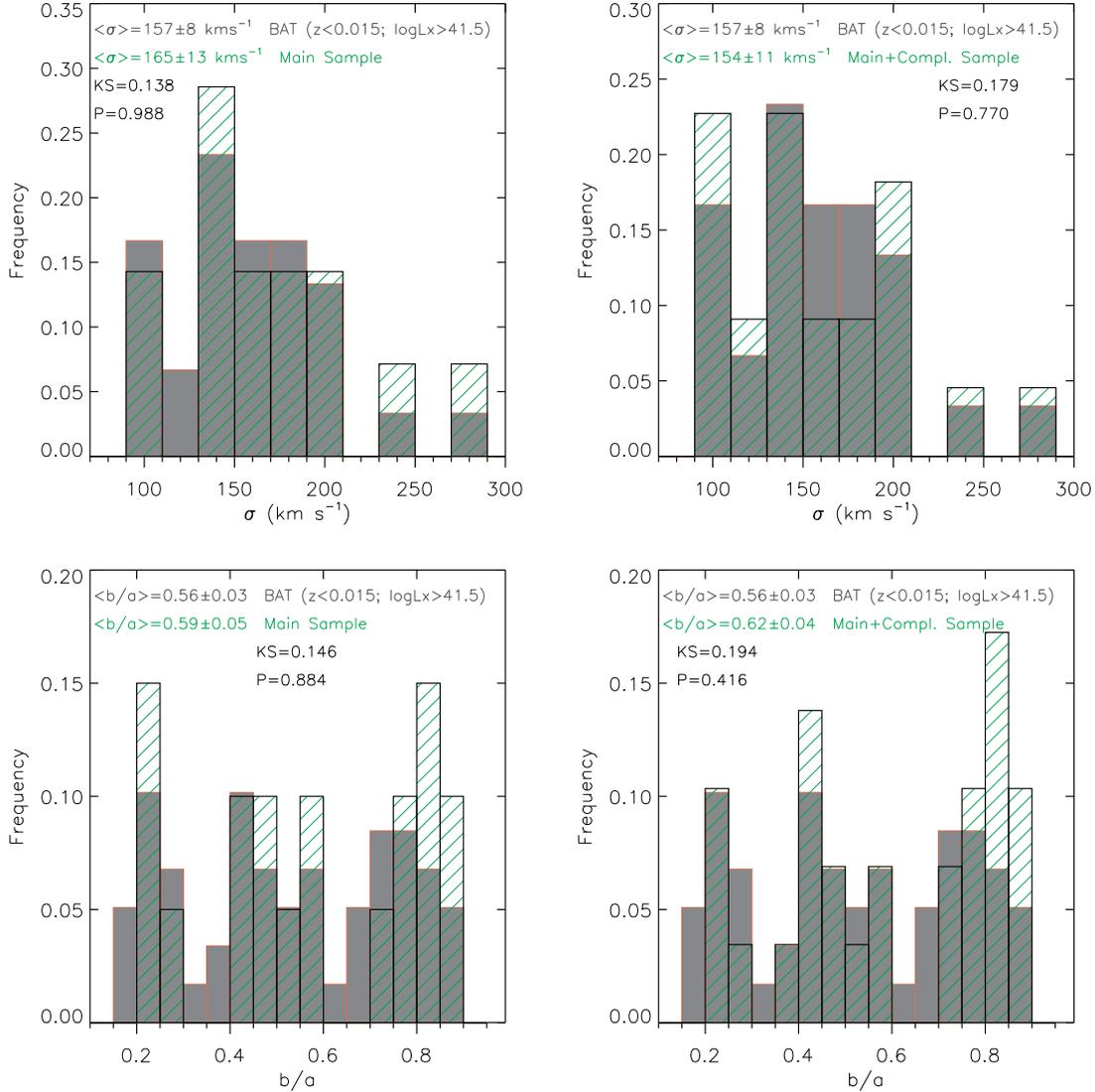
Figure 4. Distribution of central stellar velocity dispersion (top) and axial ratio (bottom) for the galaxies of the main sample (left) and main+complementary sample (right). The distribution of the restricted BAT sample is shown in gray scale on the background. Bins of $20 \, \mathrm{km \, s^{-1}}$ are used in the histograms for the velocity dispersion and of 0.05 for the axial ratio. The results for the K-S statistical test (*KS* and *P*) are shown in each panel.

our main sample ($M_B = -20.75 \pm 0.16$ mag) is similar to that of the BAT sample ($M_B = -20.52 \pm 0.12$ mag), but the distributions are somewhat distinct as the BAT sample includes more low luminosity galaxies with $M_B > -20$ mag. The K-S test results gives a probability of $\sim 33\%$ that the main and restricted BAT samples follow the same distribution in M_B, while including the complementary sample, this probability increases to $\sim 36\%$, being still small.

The total H absolute magnitude was obtained from the apparent H magnitudes from the The Two Micron All Sky Survey catalogue[3] (2MASS, Skrutskie et al. 2006). The H band is dominated by emission from the galaxy bulges and its luminosity can be used as a proxy for stellar mass of the galaxy (Davies et al. 2015, 2017). As for M_B, the dis-

tribution of the galaxies of our main sample is similar to that of the composite sample and the mean value of M_H for both samples are very similar to that observed for the BAT sample. However, for M_H the K-S test indicates that there about 68% of probability of both samples follow the same distribution. A similar P value is found if we include the complementary sample.

In Figure 4 we show histograms for the distribution of the nuclear stellar velocity dispersion (σ – top panels) and axial ratio (b/a – bottom panels). The σ values were obtained from the Hyperleda database and are standardized to an aperture of $0.595 \, h^{-1}$ kpc. Measurements of σ are available at Hyperleda database for 30 galaxies of the restricted BAT sample, 14 galaxies of the main sample and 8 objects of the complementary sample. The histograms for σ were constructed using bins of $20 \, \mathrm{km \, s^{-1}}$. As seen in

---

[3] Available at $http://vizier.u-strasbg.fr/viz-bin/VizieR$

Fig. 4 the distribution of σ values for the main and restricted BAT samples are similar, with mean σ values of $<\sigma> = 165 \pm 13 \, \text{km s}^{-1}$ and $<\sigma> = 157 \pm 8 \, \text{km s}^{-1}$, respectively. By including the complementary sample, the fraction of objects with $\sigma \leq 120 \, \text{km s}^{-1}$ increases, while the mean σ values are still consistent with that of the restricted BAT sample, as observed at the top-right panel of Fig. 4. The K-S test returns $P = 0.988$, meaning that the restricted BAT and main samples follow the same distribution in σ (with almost 99 % of probability), while including the complementary sample, this probability decreases to 77 %, being still high.

Considering that the central σ values are representative of the bulge of the galaxies, we can use the $M_\bullet - \sigma$ relation (e.g. Ferrarese & Merritt 2000; Gebhardt et al. 2000; Tremaine et al. 2002; Ferrarese & Ford 2005; Graham et al. 2011) to determine the mass of the central supermassive black hole ($M_\bullet$). Using equation 3 from Kormendy & Ho (2013) and the σ values from Fig. 4, we obtain $(0.15 \lesssim M_\bullet \lesssim 13.5) \times 10^8 \, \text{M}_\odot$ and mean values of $<M_\bullet> \approx 1.3 \times 10^8 \, \text{M}_\odot$ for the main sample and $<M_\bullet> \approx 9.8 \times 10^7 \, \text{M}_\odot$ including the complementary sample.

The main goals of our project are to map and quantify AGN feeding and feedback process via gas inflows and outflows. While inflows are usually restricted to the plane of the galaxy disk (e.g. Riffel et al. 2008; Riffel, Storchi-Bergmann & Winge 2013), outflows do not show any preferential orientation (Schmitt et al. 2001; Barbosa et al. 2014; Schönell et al. 2017). Thus, in order to optimize the search for inflows and outflows, it is desirable that the sample of galaxies show a wide range of disk orientations. The bottom panels of Figure 4 show histograms for the axial ratio b/a for our sample and restricted BAT sample (where a and b are the semi-major and semi-minor axes of the galaxy obtained from the Hyperleda database, measured at the isophote 25 mag/arcsec^2 in the B-band surface brightness distribution). Measurements of the axial ratio are available for all galaxies of our sample and for 59 objects of the restricted BAT sample. The bottom panels of Fig. 4 show histograms for the axial ratio in bins of 0.05. The mean values of b/a of our main samples are similar to that of the restricted BAT sample and including the complementary sample. Our sample shows a wide range of axial ratios, from nearly edge-on galaxies ($b/a \sim 0.2$, corresponding to a disk inclination $i \sim 80°$) to nearly face-on galaxies ($b/a \sim 0.9$, $i \sim 25°$). The K-S test shows a probability of 88 % of the main and restricted BAT samples follow the same distribution in axial ratio, while including the complementary sample, the K-S test results in $P = 0.416$, suggesting that the complementary sample includes a bias in the axial ratio distribution.

2.3 Observations

The Integral Field Spectroscopic observations of the galaxies of our sample have been obtained with the Gemini Near-Infrared Integral Field Spectrograph (NIFS, McGregor et al. 2003) operating with the Gemini North adaptive optics module ALTAIR. NIFS has a square field of view of $\approx 3''0 \times 3''0$, divided into 29 slices with an angular sampling of $0''1 \times 0''04$. The observations of our sample are part of a Large and Long Program (LLP) approved by Brazilian National Time Al-

location Committee (NTAC) and have started in semester 2015A and are planned to be concluded in 2019B. Some galaxies shown in Table 1 were observed as part of previous proposals by our group. The data comprise J and K(K$_l$)-band observations at angular resolutions in the range $0''12$–$0''20$, depending on the performance of the adaptive optics module and velocity resolution of about $40 \, \text{km s}^{-1}$ at both bands.

Emission lines from high, low-ionization and molecular gas, as well as strong CO absorptions, are usually observed at these spectral bands in spectra of active galaxies (e.g. Riffel, Rodríguez-Ardila & Pastoriza 2006), allowing the mapping of the gas kinematics, distribution, excitation, extinction and the stellar kinematics. The relatively high spatial and spectral resolutions, together with the spatial coverage, make this an unprecedented data set to map the AGN feeding and feedback processes in nearby galaxies. The on-source exposure time for each galaxy is in the range 0.7–1.7 hours at each band, expected to result in a signal-to-noise ratio $snr > 10$, which allows the fitting of the emission and absorption lines. The observations have been following the standard object-sky-object dithering sequence and the data reduction have been done following the standard procedures of spectroscopic data treatment.

2.4 Data reduction

The data reduction for the J and K band are being performed following the same procedure used in previous works (e.g. Riffel et al. 2008; Diniz et al. 2015; Riffel et al. 2017), including the trimming of the images, flat-fielding, sky subtraction, wavelength and s-distortion calibrations and correction of the telluric absorptions. The spectra are then flux calibrated by interpolating a black body function to the spectrum of the telluric standard star. Finally, datacubes for each individual exposure are created with an angular sampling of $0''05 \times 0''05$. These cubes are then mosaicked using the continuum peak as reference and median combined to produce a single final datacube for each band.

Table 2 presents a summary of the observation logs for the galaxies already observed. The angular resolution at J (PSF$_J$) and K (PSF$_K$) was estimated by measuring the full width at half maximum (FWHM) of the telluric standard star flux distributions. The uncertainties in the measurements are about $0''03$ for all galaxies at both bands. The spectral resolution at the J and K band was estimated from the FWHM of emission lines of the Ar and ArXe lamps used to wavelength calibration, respectively. For the J band we fitted the profiles of typical lines observed near 1.25 μm, while for the K band the spectral resolution was estimated from lines seen around 2.2 μm. The spectral resolution ranges from 1.7 to 2.0 Å at the J band, corresponding to an instrumental broadening ($\sigma_{inst} = \frac{FWHM}{2.355} \frac{c}{\lambda_c}$) of 17–20 km s^{-1}. At the K band the spectral resolutions ranges from 3 to 3.7 Å, translating into $\sigma_{inst} \approx 17 - 21 \, \text{km s}^{-1}$.

3 MOLECULAR AND IONIZED GAS SURFACE MASS DENSITY

We use the available data to discuss the radial distribution of ionized and molecular gas for galaxies already ob-

Table 2. Observations. (1) Galaxy name; (2) Gemini project identification; (3) J and (4) K-band on-source exposure time; (5) J and (6) K-band angular resolution estimated from the FWHM of the flux distribution of the telluric standard star; (7) J and (8) K-band spectral resolution estimated from the FWHM of the Arc Lamp lines used for wavelength calibrate the datacubes; (9) References to published studies using this dataset.

(1) Galaxy	(2) Programme	(3) J Exp. T. (seconds)	(4) K Exp. T. (seconds)	(5) PSF$_J$ (arcsec)	(6) PSF$_K$ (arcsec)	(7) FWHM$_J$ (Å)	(8) FWHM$_K$ (Å)	(9) Refs.
Main sample								
NGC788	GN-2015B-Q-29	7×400	11×400	0.13	0.13	1.9	3.5	a
NGC1068	GN-2006B-C-9*	27×90	27×90	0.14	0.11	1.7	3.0	b, c, d
NGC2110	GN-2015B-Q-29	6×400	–	0.13	–	1.9	–	a, e
–	GN-2010B-Q-25		6×600	0.15	–	–	3.4	–
Mrk3	GN-2010A-Q-5*	6×600	6×600	0.13	0.13	2.0	3.2	–
NGC3227	GN-2016A-Q-6	6×400	6×400	0.13	0.12	1.8	3.5	a
NGC3516	GN-2015A-Q-3	10×450	10×450	0.17	0.15	1.8	3.5	a
NGC4151	GN-2006B-C-9*	8×90	8×90	0.16	0.12	1.6	3.3	f, g, h
NGC4235	GN-2016A-Q-6	9×400	10×400	0.12	0.13	1.8	3.5	a
Mrk766	GN-2010A-Q-42	6×550	6×550	0.21	0.19	1.7	3.5	a, j
NGC4388	GN-2015A-Q-3	–	2×400	–	0.19	–	3.7	a
NGC5506	GN-2015A-Q-3	10×400	10×400	0.15	0.18	1.9	3.6	a
Complementary Sample								
NGC1052	GN-2010B-Q-25	6×610	4×600		0.15	1.7		a
NGC4051	GN-2006A-SV-123	–	6×750	–	0.18	–	3.2	a, k
NGC5548	GN-2012A-Q-57	12×450	12×450	0.28	0.20	1.7	3.5	a, l
NGC5899	GN-2013A-Q-48	10×460	10×460	0.13	0.13	1.8	3.4	a
NGC5929	GN-2011A-Q-43	10×600	10×600	0.12	0.12	1.7	3.2	a, m, n
Mrk79	GN-2010A-Q-42	6×520	6×550	0.25	0.25	1.8	3.5	o
Mrk607	GN-2012B-Q-45	10×500	12×500	0.14	0.14	2.0	2.2	a
Mrk1066	GN-2008B-Q-30	8×600	8×600	0.13	0.15	1.7	3.3	a, p, q, r, s
Mrk1157	GN-2009B-Q-27	8×550	8×550	0.11	0.12	1.8	3.5	a, t, u

* From Gemini Science Archive

References: a: Riffel et al. (2017); b: Storchi-Bergmann et al. (2012); c: Riffel et al. (2014); d: Barbosa et al. (2014);
e: Diniz et al. (2015); f: Storchi-Bergmann et al. (2009), g: Storchi-Bergmann et al. (2010);
h: Riffel, Storchi-Bergmann & McGregor (2009); i: Schönell et al. (2014); k: Riffel et al. (2008); l: Schönell et al. (2017);
m: Riffel, Storchi-Bergmann & Riffel (2014); n: Riffel, Storchi-Bergmann & Riffel (2015);
o: Riffel, Storchi-Bergmann & Winge (2013); p: Riffel et al. (2010); q: Riffel, Storchi-Bergmann & Nagar (2010);
r: Riffel & Storchi-Bergmann (2011a); s: Ramos Almeida et al. (2014); t: Riffel et al. (2011c);
u: Riffel & Storchi-Bergmann (2011b).

served. The fluxes of the $H_2\lambda 2.12\,\mu$m and Brγ emission lines can be used to estimate the mass of hot molecular and ionized gas, respectively. Following Osterbrock & Ferland (2006) and Storchi-Bergmann et al. (2009), the mass of ionized (M_{HII}) gas can be obtained from

$$\left(\frac{M_{HII}}{M_\odot}\right) = 3\times 10^{19}\left(\frac{F_{Br\gamma}}{\mathrm{erg\,cm^{-2}\,s^{-1}}}\right)\left(\frac{D}{\mathrm{Mpc}}\right)^2\left(\frac{N_e}{\mathrm{cm^{-3}}}\right)^{-1},\tag{1}$$

where D is the distance to the galaxy, $F_{Br\gamma}$ is the Brγ flux and N_e is the electron density, assuming an electron temperature of 10^4K. We have adopted an electron density of $N_e = 500\,\mathrm{cm^{-3}}$, which is a typical value for the inner few hundred pcs of AGNs as determined from the [S II]$\lambda\lambda 6717,6730$ lines (e.g. Dors et al. 2014; Brum et al. 2017).

Under the assumptions of local thermal equilibrium and excitation temperature of 2000 K, the mass of hot molecular

gas (M_{H2}) can be obtained from (e.g. Scoville et al. 1982; Riffel et al. 2014):

$$\left(\frac{M_{H_2}}{M_\odot}\right) = 5.0776\times 10^{13}\left(\frac{F_{H_2\lambda 2.1218}}{\mathrm{erg\,s^{-1}\,cm^{-2}}}\right)\left(\frac{D}{\mathrm{Mpc}}\right)^2,\tag{2}$$

where $F_{H_2\lambda 2.1218}$ is the H_2 (2.1218μm) emission-line flux.

We used the equations 1 and 2 to calculate the molecular and ionized gas mass density spaxel-by-spaxel by defining the gas surface mass densities of the molecular and ionized gas as $\Sigma_{H2} = \frac{M_{H_2}}{A_s}$ and $\Sigma_{HII} = \frac{M_{HII}}{A_s}$, respectively, where A_s is the area of each spaxel. Using the calculated values of Σ_{H2} and Σ_{HII} we constructed the surface mass density profiles shown in Figures 5–9. Following Barbosa et al. (2006), we calculated the position (r) of each spaxel in the plane of the disk as $r = \alpha R$, where

$$R = \sqrt{(x-x_0)^2+(y-y_0)^2}$$

is the position projected in the plane of the sky (observed

position) and

$$\alpha = \sqrt{\cos^2(\Psi - \Psi_0) + \sin^2(\Psi - \Psi_0)/\cos^2(i)},$$

where Ψ_0 is the orientation of the line of nodes, i is the disk inclination and $\Psi = \tan^{-1}\left(\frac{y - y_0}{x - x_0}\right)$ with (x, y) being the spaxel coordinates and (x_0, y_0) the location of the kinematical center. Then, the surface mass density profiles were constructed by averaging the surface mass densities within concentric rings in the galaxy plane with width of $dr = 25$ pc. For all galaxies we fixed the (x_0, y_0) as the position of the continuum peak and included only spaxels with flux measurements for the corresponding emission lines. For most galaxies, the $H_2\lambda2.12\,\mu$m and Brγ flux maps have already been published by our group in the references listed in the last column of Table 2. Although the Brγ line is weaker than Paβ, its use is justified due to the fact that using Brγ and $H_2\lambda2.12$ lines, both ionized and molecular masses are derived from the same spectral band and thus the ratio between them is less sensitive to uncertainties in the flux calibrations and extinction, as both lines are are close in wavelength. For two galaxies (NGC 1052 and NGC 5548), the Brγ line was not detected in our spectra and thus we used the Paβ emission line to estimate M_{HII} by assuming the theoretical ratio between the fluxes of Paβ and Brγ of 5.85 for the Case B recombination (Osterbrock & Ferland 2006). The references for the corresponding measurements as well as the discussion about the fitting procedures are listed in the last column of Table 3. This table presents also the adopted Φ_0 and i values, most of them from Riffel et al. (2017), who obtained these values by fitting the observed stellar velocity fields by rotation disk models and from the application of the technique of kinemetry to the measured kinematics. For Mrk 3 and Mrk 79 we used the disk geometric parameters from the Hyperleda database (Makarov et al. 2014), for NGC 1068 from Davies et al. (2007) and for NGC 4151 those presented in Onken et al. (2014).

The top panels of figures 5–9 present for each galaxy the profiles for Σ_{H2} in black, in units of $10^{-3}\,M_\odot\,\mathrm{pc}^{-2}$, and Σ_{HII} in red in units of $M_\odot\,\mathrm{pc}^{-2}$. The dotted blue line represents the K-band surface brightness profile obtained from a continuum image derived by averaging the fluxes between 2.23 and 2.30 μm. This profile is shown in units of $C\times$erg s^{-1} cm^{-2} Å^{-1} arcsec^{-2} – where C is an arbitrary constant to put the profile in similar units to those of the mass density profiles – to be used as a tracer of the stellar mass distribution. The bottom panel shows the ratio between Σ_{HII} and Σ_{H2} or equivalently $\frac{M_{HII}}{M_{H_2}}$, calculated considering only spaxels in which both Brγ and $H_2\lambda2.12$ flux measurements are available. The dotted horizontal line shows the mean value of $\frac{M_{HII}}{M_{H_2}}$, indicated at the top-right corner of this panel and calculated from the Σ_{HII}/Σ_{H2} profile. The dashed lines represent the standard error, calculated as the ratio between the standard deviation of the Σ at each ring and the number of spaxels used to compute Σ.

For all galaxies, the ionized and molecular gas mass density profiles decrease with the distance to the nucleus, with the ionized gas showing a steeper gradient for most galaxies. This behavior can be attributed to the different nature of the excitation mechanisms for the ionized and molecular gas: while the former is excited by the AGN radiation, the latter is dominated by thermal excitation through heating

of the surrounding gas by X-rays emitted by the AGN (e.g. Dors et al. 2012; Riffel et al. 2013; Colina et al. 2012). As X-rays are less blocked by the surrounding gas, they penetrate in the disk more uniformly in all directions, so that the H_2 flux distributions are also more uniform than those of the ionized gas. The ionized gas usually shows more collimated flux distributions, as the AGN UV radiation is at least partially blocked by the dusty torus. The only exception is NGC 1068, that shows an increase in Σ_{H2} between 25 and 75 pc due to the presence of an expanding molecular gas ring (e.g. Müller-Sánchez et al. 2009; Riffel et al. 2014; Barbosa et al. 2014). Both the ionized and molecular surface density profiles usually decrease more slowly with distance from the nucleus than the K-band brightness profile. The fact that the gas mass density profiles are less steep than the stellar brightness profile is probably due to the fact that the gas has (more recently than the stars) settled in a disc, while the stellar density profile is dominated by stars from the galaxy bulge. The bottom panels for each galaxy shows the radial profile for $\frac{M_{HII}}{M_{H_2}}$, that confirm the trend that ionized gas shows an steeper decrease in surface mass density than the molecular gas, as the $\frac{M_{HII}}{M_{H_2}}$ for most galaxies have the highest values at the nucleus or at small distances from it. The mean values of $<\frac{M_{HII}}{M_{H_2}}>$, indicated at the top-left corner of each panel, range from $\sim$200 for Mrk 607 to $\sim$8000 for NGC 5506.

Table 3 shows the total mass of ionized and hot molecular gas for each galaxy by summing up the masses from all spaxels with detected Brγ and $H_2\lambda2.12\,\mu$m emission. The uncertainties in the masses are not included in this table, they are dominated by the uncertainty in flux calibration and can be up to 20 %. The mass of ionized gas is in the range $(3-440)\times10^4\,M_\odot$, while that for the hot molecular gas ranges from 50 to 3 000 $M_\odot$. The mean surface mass density for the ionized and molecular gas, shown in Table 3 are in the ranges $(0.2-35.9)\,M_\odot\,\mathrm{pc}^{-2}$ and $(0.2-13.9)\times10^{-3}\,M_\odot\,\mathrm{pc}^{-2}$. These values are in good agreement with those previously obtained, summarized by Schönell et al. (2017) in their Table 1. The distribution of ionized and molecular masses and surface mass densities for the galaxies of our sample are presented in Figure 10.

In order to further investigate the distribution of ionized and molecular gas in the inner few hundreds of parsercs of the galaxies of our sample, we constructed normalized radial profiles by dividing the M_{HII}/M_{H2} value at each radial bin by the nuclear value ($r < 25$ pc). These profiles are shown in Figure 11. Seyfert 1 galaxies (Mrk 766, Mrk 79, NGC 3227, NGC 3516, NGC 4051, NGC 4151 and NGC 5548) are shown as red continuous lines and Seyfert 2 galaxies (Mrk 1066, Mrk 1157, Mrk 3, Mrk 607, NGC 1052, NGC 1068, NGC 2110, NGC 4388, NGC 5506, NGC 5899, NGC 5929, NGC 788) as blue dashed lines. These profiles confirm the result already mentioned above that the ionized gas has an steeper surface mass profile, as for most galaxies the M_{HII}/M_{H2} decreases with the distance to the nucleus. In addition, Figure 11 shows that there is no significant difference for the distribution of ionized and molecular gas for Seyfert 1 and Seyfert 2 nuclei.
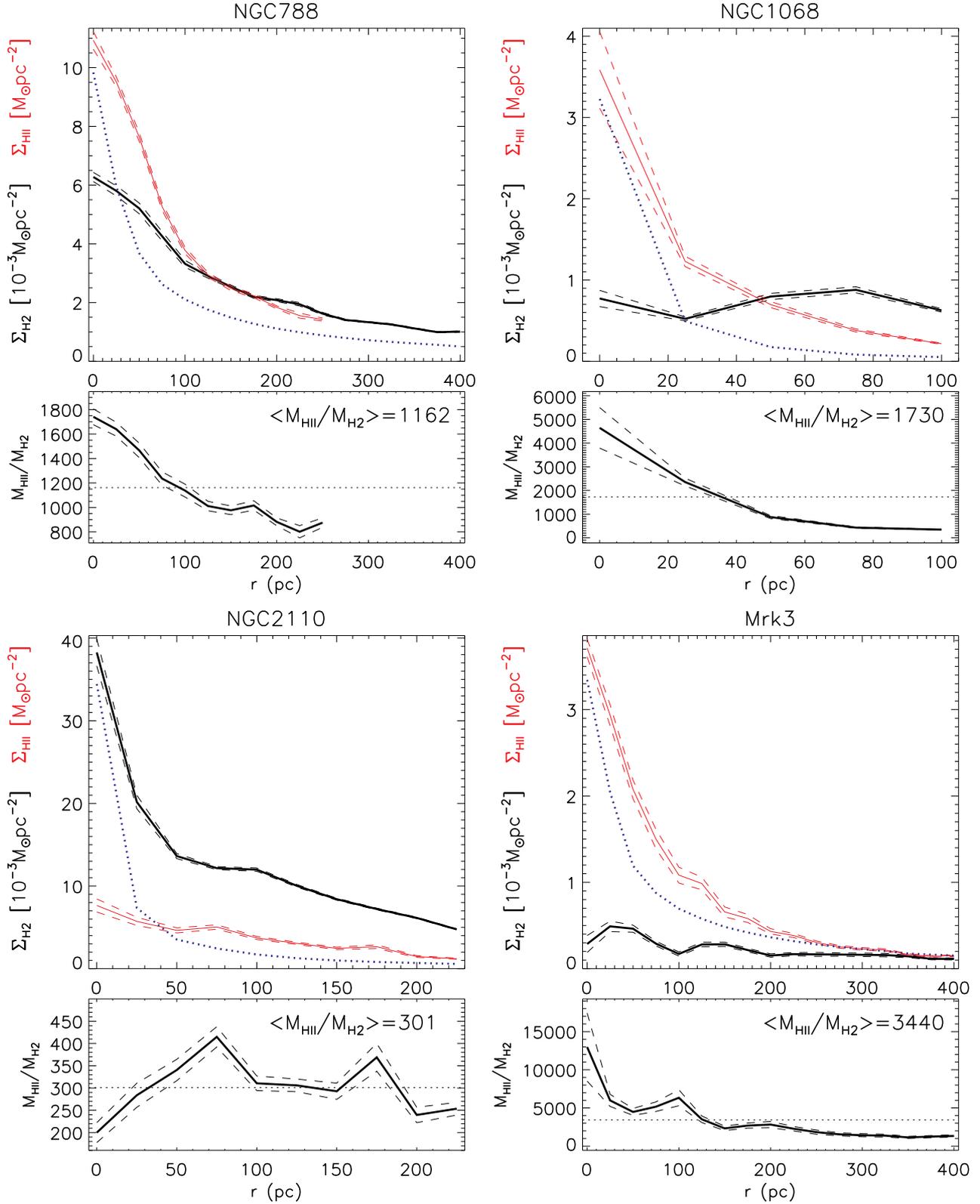
Figure 5. The top panels show the surface mass density profiles for the hot molecular (black) and ionized (red) for a radial bin of 25 pc at the plane of the galaxy. The profiles are shown as continuous lines and the dashed lines shows the standard error variation. The K-band surface brightness is shown as a dotted blue line in units of $C \times$ erg s^{-1} cm^{-2} Å^{-1} arcsec^{-2}, where C is an arbitrary constant. The bottom panels show the ratio ratio between the mass of ionized and molecular gas variation for the same radial bin, considering only spaxels with measurements of both masses. The mean value of the ratio $< M_{HII}/M_{H2} >$ is shown at the top-right corner of the corresponding panel. The geometric parameters of the disk, used in the deprojection are shown in Table 3. In this figure, we show the profiles for NGC 788, NGC 1068, NGC 2110 and Mrk 3.
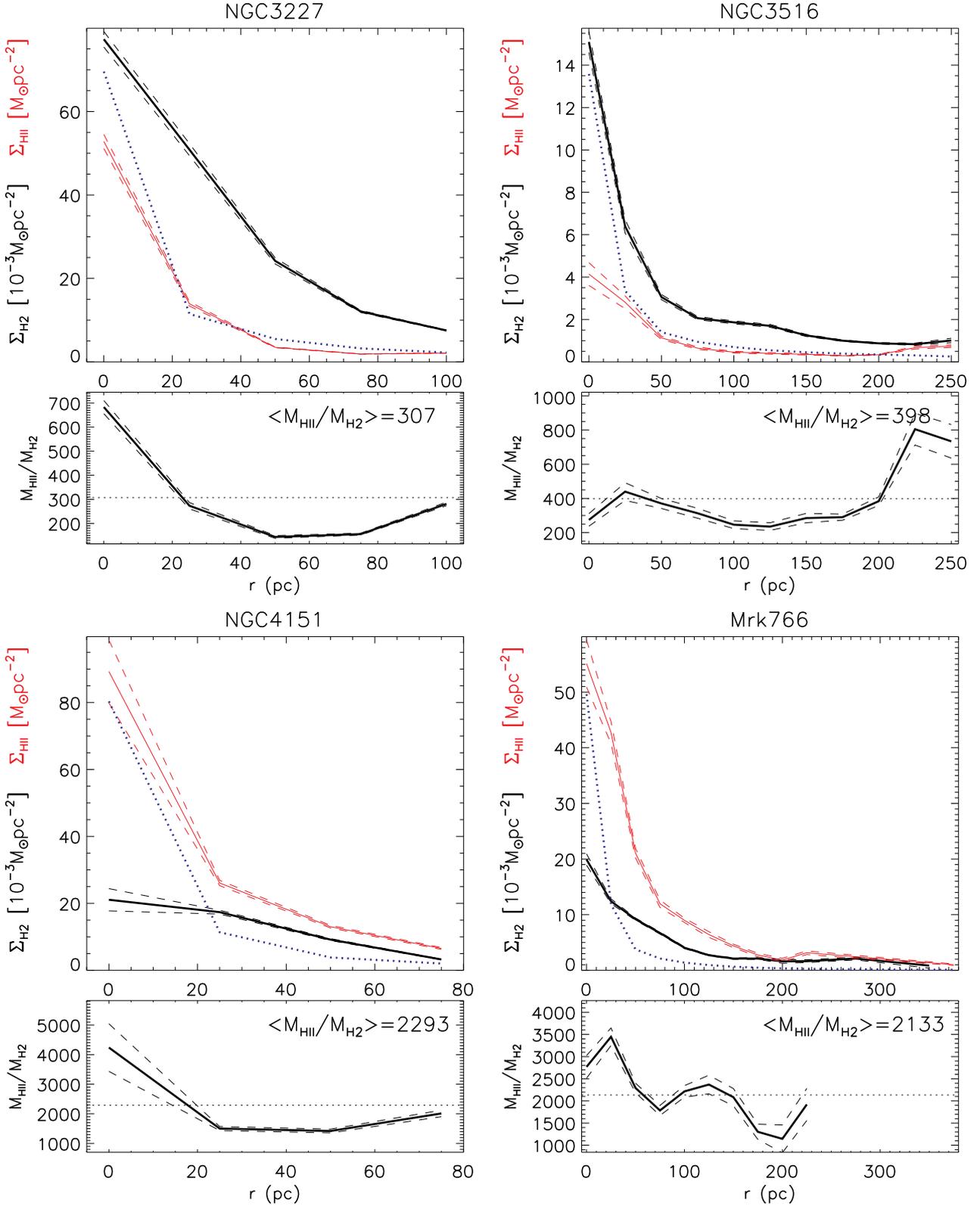
Figure 6. Same as Fig. 5 for NGC 3227, NGC 3516, NGC 4151 and Mrk 766.
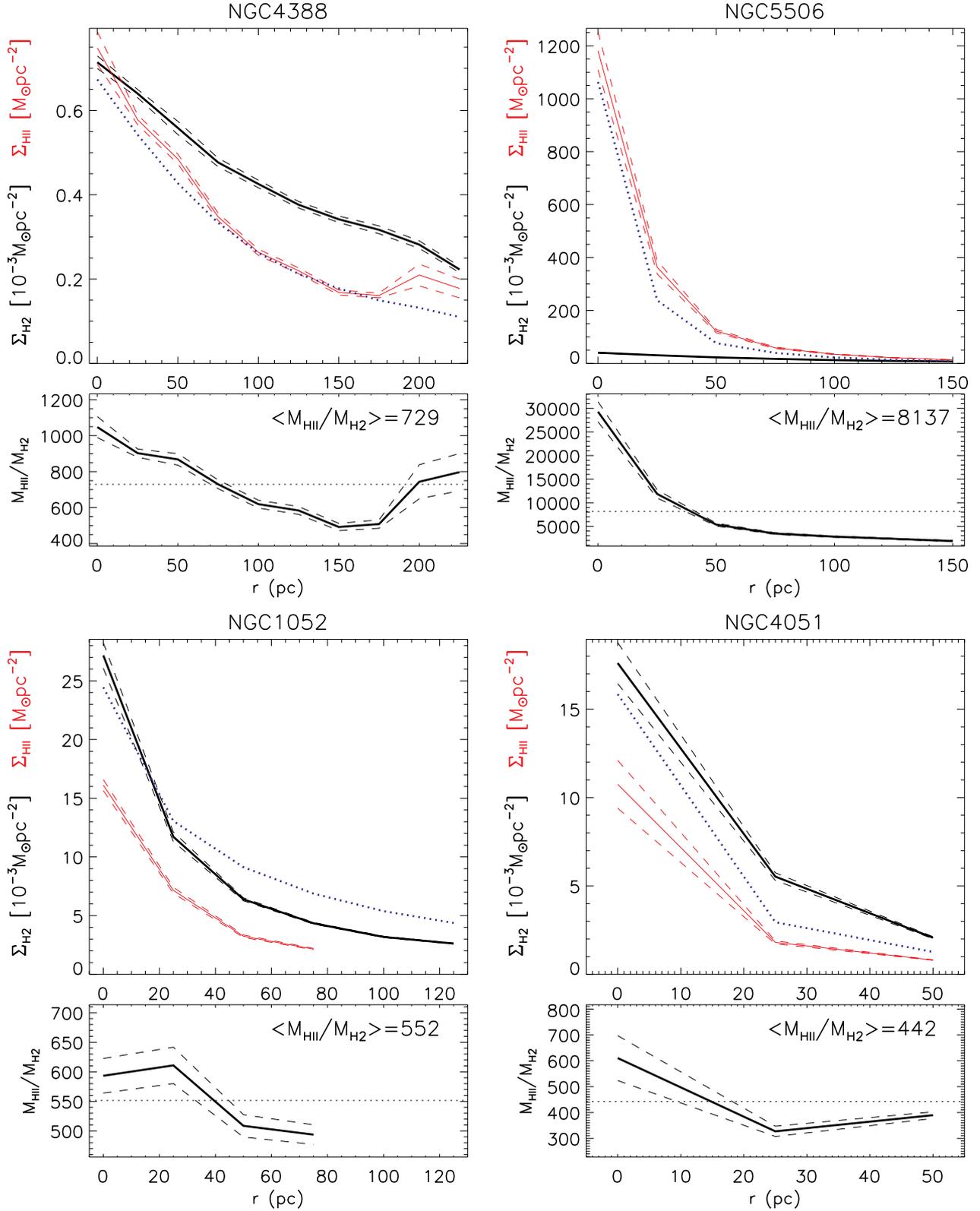
Figure 7. Same as Fig. 5 for NGC 4388, NGC 5506, NGC 1052 and NGC 4051.
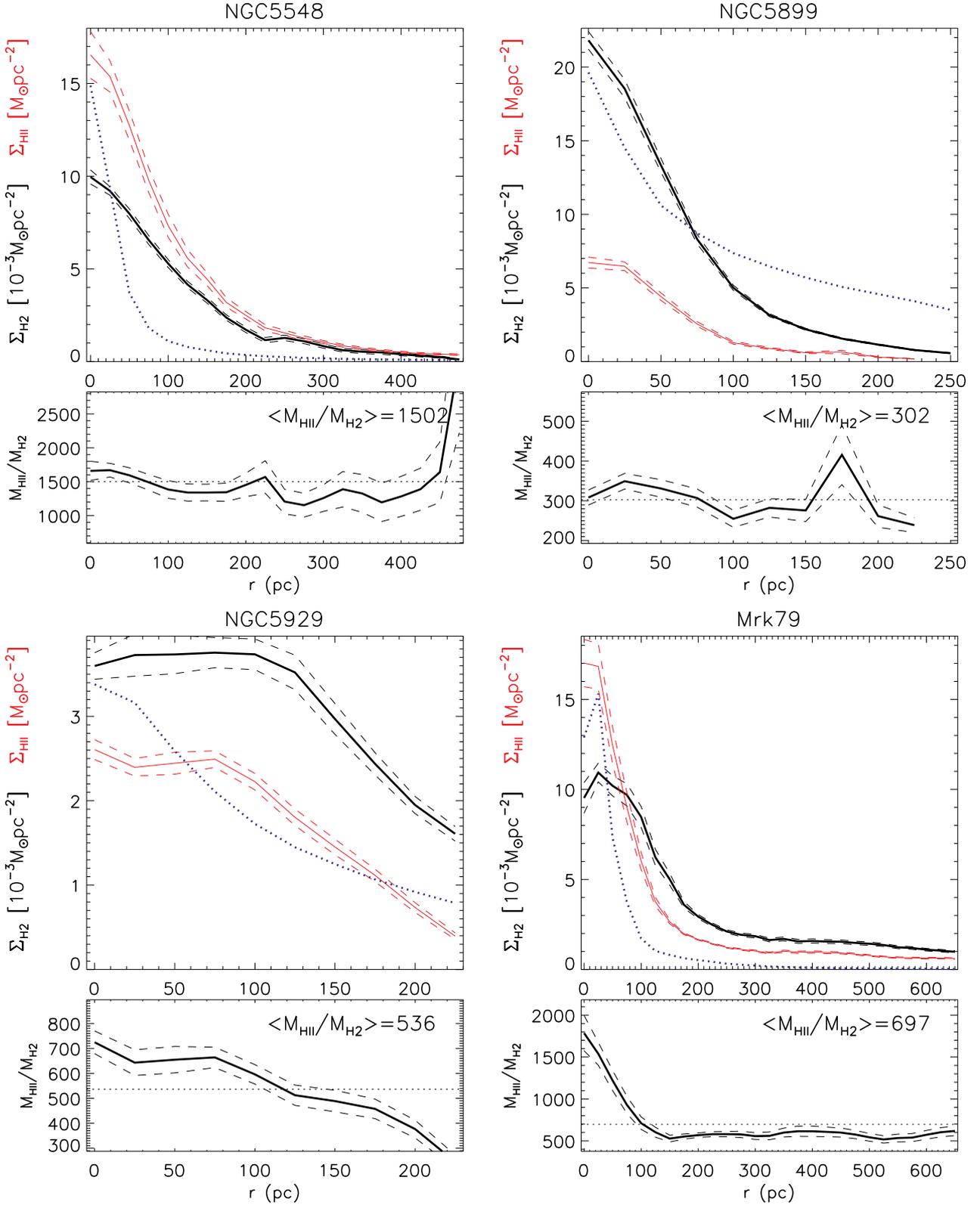
Figure 8. Same as Fig. 5 for NGC 5548, NGC 5899, NGC 5929 and Mrk 79.
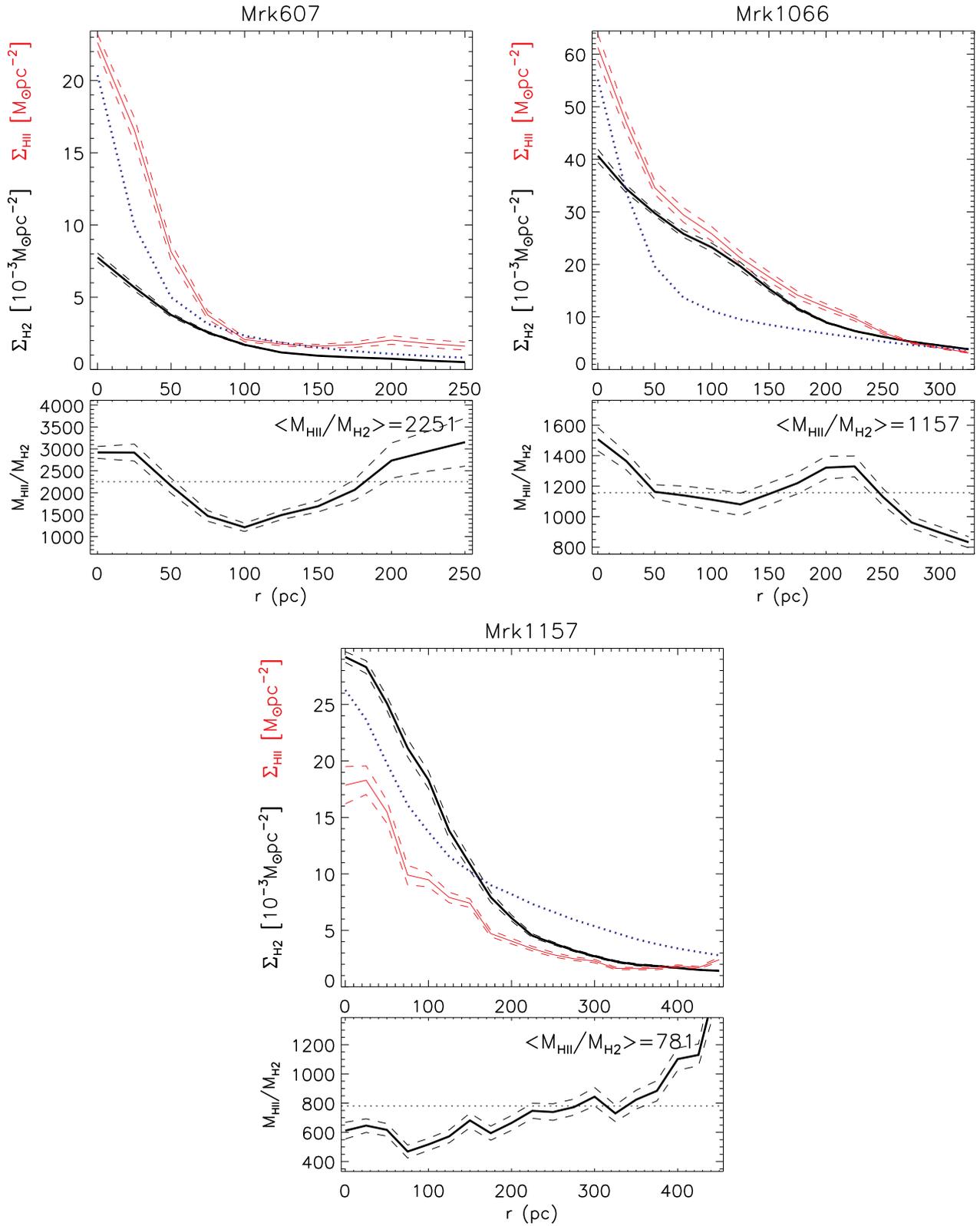
Figure 9. Same as Fig. 5 for Mrk 607, Mrk 1066 and Mrk 1157.
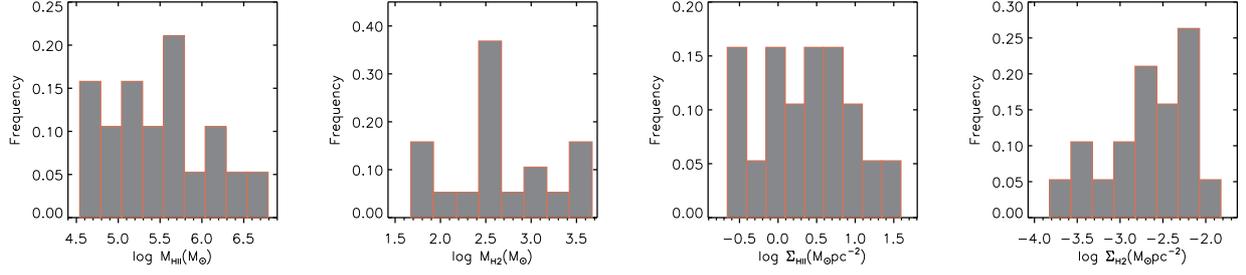
Figure 10. Histograms for M_{HII}, Σ_{HII}, M_{H2} and Σ_{H2} for our sample, constructed using the values from Table 3 using a bin of 0.25 dex.

Table 3. Molecular and ionized gas masses and surface densities. (1) Name of the galaxy; (2) Total mass of ionized gas; (3) Area for the Brγ emission; (4) Average surface mass density for the ionized gas; (5) Total mass of hot molecular gas; (6) Area for the H$_2\,\lambda 2.12$ emission; (7) Average surface mass density for the hot molecular gas; (8) Average star formation density; (9) total star formation rate; (10) and (11) orientation of the major axis and inclination of the disk, used in the deprojection from Riffel et al. (2017), except for Mrk 3 and Mrk 79 (from Hyperleda database Makarov et al. 2014), NGC 1068 (from Davies et al. 2007) and NGC 4151 (from Onken et al. 2014); (12) AGN bolometric luminosity estimated from the 14-195 keV luminosity; (13) mass accretion rate onto the SMBH; (14) Reference for the H$_2\,\lambda 2.12$ and Brγ flux maps.

(1) Galaxy	(2) M_{HII} $10^4 M_\odot$	(3) A_{HII} $10^4 pc^2$	(4) $<\Sigma_{HII}>$ $M_\odot/pc^2$	(5) M_{H2} $10^2 M_\odot$	(6) A_{H2} $10^4 pc^2$	(7) $<\Sigma_{H2}>$ $10^{-3} M_\odot/pc^2$	(8) $<\Sigma_{SFR}>$ $10^{-3} M_\odot/yr\,kpc^2$	(9) SFR $10^{-4} M_\odot/yr$	(10) Ψ_0 deg	(11) i deg	(12) $\log L_{bol}$ erg/s	(13) $\dot{m}$ 10^{-3} $M_\odot/yr$	(14) Ref.
Main Sample													
NGC788	36.11	8.30	4.35	10.90	70.25	1.55	1.96	1.63	120	20.8	44.4	49.2	a
NGC1068	3.47	15.59	0.22	0.54	15.86	0.34	0.03	0.05	145	40.0	42.8	1.1	b
NGC2110	28.17	11.00	2.56	15.66	23.79	6.59	0.93	1.03	156	42.5	44.6	65.4	c
Mrk3	22.39	59.90	0.37	0.47	31.03	0.15	0.06	0.38	15	31.7	44.7	87.2	d
NGC3227	17.87	2.69	6.64	7.81	5.95	13.12	3.54	0.95	156	45.4	43.4	4.1	a
NGC3516	11.62	15.94	0.73	3.87	30.63	1.26	0.16	0.26	54	12.8	44.2	27.9	a
NGC4151	59.22	5.93	9.99	2.87	5.72	5.02	6.27	3.72	85	23.0	44.0	16.0	e
Mrk766	51.60	2.93	17.60	3.75	6.53	5.74	13.85	4.06	66	18.2	44.0	16.0	f
NGC4388	4.36	18.37	0.24	0.67	22.31	0.30	0.03	0.06	96	27.7	44.6	65.4	a
NGC5506	439.64	12.26	35.86	8.89	12.00	7.41	37.53	46.01	96	58.7	44.3	37.0	a
Complementary Sample													
NGC1052	6.18	0.92	6.70	3.00	7.56	3.96	3.58	0.33	114	47.5	42.9	1.4	g
NGC4051	3.64	2.13	1.71	0.86	2.91	2.94	0.53	0.11	24	37.3	42.5	0.5	h
NGC5548	74.49	85.30	0.87	3.80	15.70	2.42	0.21	1.76	108	60.9	44.7	87.2	i
NGC5899	8.10	3.81	2.12	3.60	23.45	1.53	0.72	0.27	24	62.7	43.1	2.4	a
NGC5929	14.70	23.77	0.62	3.94	28.86	1.37	0.13	0.30	30	60.7	–	–	j
Mrk79	169.24	163.24	1.04	26.90	179.32	1.50	0.26	4.29	73	35.6	44.8	116.4	k
Mrk607	51.85	20.30	2.55	2.06	28.49	0.72	0.93	1.89	138	58.2	–	–	a
Mrk1066	305.89	31.45	9.73	30.11	45.02	6.69	6.04	19.0	120	50.2	–	–	l
Mrk1157	188.70	65.13	2.90	28.24	89.60	3.15	1.11	7.22	114	45.1	–	–	m

a: Schonell et al., in prep.; b: Riffel et al. (2014); c: Diniz et al. (2015) ; d: Fischer et al., in prep.; e: Storchi-Bergmann et al. (2009)
f: Schönell et al. (2014); g: Dahmer-Hahn et al, in prep.; h: Riffel et al. (2008); i: Schönell et al. (2017); j: Riffel, Storchi-Bergmann & Riffel (2015);
k: Riffel, Storchi-Bergmann & Winge (2013); l: Riffel, Storchi-Bergmann & Nagar (2010); m: Riffel & Storchi-Bergmann (2011b)

4 FEEDING THE AGN AND STAR FORMATION

We can estimate the accretion rate ($\dot{m}$) to the AGN in each galaxy by

$$\dot{m} = \frac{L_{bol}}{c^2 \eta}, \qquad (3)$$

where L_{bol} is the AGN bolometric luminosity, c is the light speed and η is the efficiency of conversion of the rest mass energy of the accreted material into radiation. The AGN bolometric luminosity can be estimated from the hard X-ray luminosity by (Ichikawa et al. 2017)

$$\log L_{bol} = 0.0378(\log L_X)^2 - 2.03\log L_X + 61.6, \qquad (4)$$

where L_X is the hard X-ray (14-195 keV) luminosity. The resulting $\dot{m}$ values using the X-ray luminosities from Table 1 and assuming $\eta \approx 0.1$ (e.g. Frank, King & Raine 2002), are shown in Table 3. The $\dot{m}$ for our sample ranges from 10^{-4} (for NGC 4051) to 10^{-1} M$_\odot$ yr^{-1} (for Mrk 79), with a mean value of $<\dot{m}> \sim 0.03$ M$_\odot$ yr^{-1}.

The surface mass density profiles of Figs. 5–9 show that most of the ionized and molecular gas masses listed in Table 3 are concentrated within the inner $\sim$300 pc of the galaxies. The ionized gas mass alone would be enough to feed the central AGN for an activity cycle of $10^7 - 10^8$ yr. The hot molecular gas mass is typically 3 orders of magnitudes lower than that of the ionized gas, but this gas is just the heated surface of a probably much larger molecular gas reservoir of colder molecular gas, that may be $10^5 - 10^7$ times
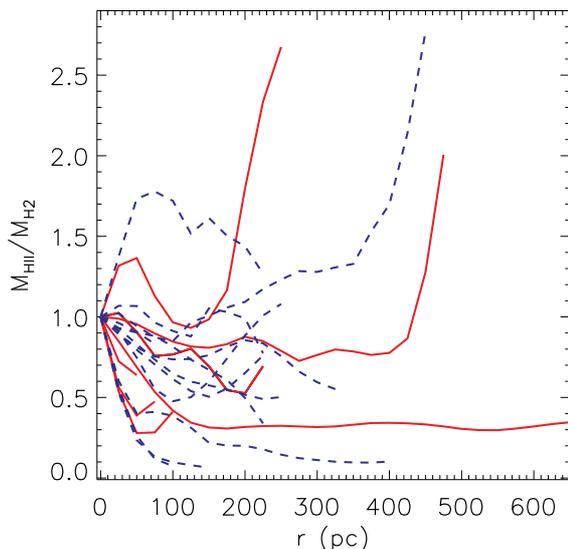
Figure 11. Normalized (by the nuclear value) radial profiles of $M_{\rm HII}/M_{\rm H2}$. Seyfert 1 galaxies are shown as continuous red lines and Seyfert 2 galaxies as dashed blue lines.

more massive (Dale et al. 2005; Müller-Sánchez 2006; Mazzalay et al. 2013), implying that the masses of the cold molecular gas probably range from $10^7 - 10^9$ M$_\odot$.

We conclude that, within the inner 300 pc of our sample, there is at least $\sim 10^2$ times more gaseous mass than the necessary to feed the AGN. Most of this mass will not feed the AGN and might be consumed by star formation. The pioneer work by Schmidt (1959) showed that the star formation rate (*SFR*) is directly related to the gas density, while Kennicutt (1998) derived a relation between the SFR surface density (Σ_{SFR}) and the ionized gas mass surface density ($\Sigma_{\rm HII}$) so that the former can be obtained from the latter as

$$\frac{\Sigma_{SFR}}{M_\odot yr^{-1} kpc^{-2}} = (2.5 \pm 0.7) \times 10^{-4} \left(\frac{\Sigma_{\rm HII}}{M_\odot pc^{-2}} \right)^{1.4}, \qquad (5)$$

where $\Sigma_{\rm HII}$ is the surface mass density.

Using the equation above, we obtained the mean values of the star formation density $<\Sigma_{SFR}>$ for each galaxy, shown in Table 3, which varies from 3×10^{-5} to 3.8×10^{-2} $M_\odot yr^{-1} kpc^{-2}$. We point out that these should be minimum values, as we are considering only the ionized gas, and there should much more molecular gas than traced by the hot molecular gas phase that we have observed. Considering the area of the Brγ emission quoted in Table 3, we obtain a wide range of minimum total star formation rate of 10^{-6}–10^{-3} M$_\odot$ yr^{-1} (shown in Table 3). These values of *SFR* are smaller smaller than those usually obtained for the nucleus of star-forming galaxies and circumnuclear rings of star formation (*SFR* $\sim 10^{-3}$ M$_\odot$ yr^{-1}) (e.g. Wold & Galliano 2006; Shi, Gu & Peng 2006; Dors et al. 2008; Galliano & Alloin 2008; Falcón-Barroso et al. 2014; Riffel et al. 2016). Considering a scenario in which the total mass would be used to form stars, the estimated masses for our sample would al-

low the star formation for about 10^9 yr at the current star formation rate.

Thus, considering the derived mass accretion rate, the star formation rate and the mass of molecular and ionized gas, we conclude that the mass reservoirs of the galaxies of our sample are much larger than that needed to power the central AGN and star formation, thus allowing the co-existence of recent star formation (as evidenced by low-stellar velocity dispersion structures seen in some galaxies, Riffel et al. 2017) and the nuclear activity.

5   CONCLUSIONS

We characterized a sample of 20 nearby X-ray selected Seyfert galaxies being observed with the NIFS instrument of the Gemini North Telescope plus a complementary sample of 9 additional galaxies already observed with NIFS. We also present and discuss mean radial profiles within the inner kiloparsec for the ionized and molecular gas surface mass densities for the galaxies already observed: 11 from the main X-ray sample and 9 galaxies from the complementary sample. Our main conclusions are:

- The average values of X-ray luminosities are $< \log L_{\rm X} > = 42.6 \pm 0.1$ erg s^{-1} for the main sample and $< \log L_{\rm X} > = 42.4 \pm 0.1$ erg s^{-1} for the main plus complementary sample. The [O III]$\lambda 5007$ luminosities are in the range $L_{[OIII]} = (0.2 - 155) \times 10^{40}$ erg s^{-1}, with a mean value of $< \log L_{[OIII]} > = 41.0 \pm 0.2$ erg s^{-1}.

- The M_B and M_H distributions for the restricted BAT sample (all galaxies with $L_X \geq 10^{41.5}$ ergs s^{-1} and $z \leq 0.015$ from the 60 month BAT catalogue) and our sample are very similar, indicating that the additional criteria used in the definition of our sample does not include any bias in terms of these properties. The mean values for our sample are $< M_B > = -20.75 \pm 0.16$ and $< M_H > = -23.83 \pm 0.13$.

- The mean value of the central stellar velocity dispersion of the total sample is 154 ± 11 km s^{-1}, being essentially the same as that of the X-ray sample only.

- The axial ratio b/a of the total sample ranges from 0.2 (corresponding to a disk inclination of $i \sim 80°$, almost edge-on) to 0.9 ($i \sim 25°$, almost face-on).

- We constructed mean radial profiles for the surface mass density of the ionized ($\Sigma_{\rm HII}$) and hot molecular ($\Sigma_{\rm H2}$) gas for the 20 galaxies already observed, derived from the Brγ and H$_2\lambda 2.12\mu m$ fluxes. Both profiles decrease with the distance from the nucleus for most galaxies, with the ionized gas showing a steeper gradient. The only exception is NGC 1068, which shows an increase in $\Sigma_{\rm H2}$ at 25–75 pc from the nucleus due to the presence of a molecular gas ring. We attribute this difference in behavior to the distinct origin of the gas emission: while for the H$^+$ the emission is due to recombination of ionized gas by the AGN, for the H$_2$ the excitation is mostly thermal due to the heating of the gas by X-rays that penetrate deeper into the surrounding gas in the galaxy plane.

- The mean surface mass density for the ionized and molecular gas are in the ranges $(0.2-35.9)$ M$_\odot$ pc^{-2} and $(0.2-13.9) \times 10^{-3}$ M$_\odot$ pc^{-2}, respectively, while the ratio between them ranges from ~ 200 for Mrk 607 to ~ 8000 for NGC 5506. The mean star formation surface density is $<$

$\Sigma_{SFR} \geq = (4.09 \pm 0.44) \times 10^{-3} M_{\odot} \, yr^{-1} \, kpc^{-2}$, while the star formation rates range from 10^{-6} to 10^{-3} $M_{\odot} \, yr^{-1}$, with the accretion rate onto the SMBH ranging from 10^{-4} to 10^{-1} $M_{\odot} \, yr^{-1}$.

• The total mass of ionized gas within the inner $\sim 100 - 500 \, pc$ is in the range $(3 - 440) \times 10^4 M_{\odot}$, while that of hot molecular gas ranges between 50 and 3000 $M_{\odot}$. Considering also that the mass of cold molecular gas is usually $\sim 10^5$ times larger than that of hot molecular gas for AGN in general, we estimate a total mass of gas in the region ranging from 10^6 to 10^8 $M_{\odot}$. Comparing these masses with the typical accretion rates above, it can be concluded that they are much larger than that necessary to feed a typical AGN cycle of of $10^7 - 10^8$ yr. The fate of this gas is probably the formation of new stars in the region (the AGN-Starburst connection).

ACKNOWLEDGMENTS

REFERENCES

Aalto, S. et al. 2012, A&A, 573, 44
Ajello, M., Alexander, D. M., Greiner, J., Madejski, G. M., Gehrels, N., Burlon, D., 2012, ApJ, 749, 21.
Audibert, A., Riffel, R., Sales, D. A., Pastoriza, M. G., Ruschel-Dutra, D., 2017, MNRAS, 464, 2139.
Barbosa, F. K. B., Storchi-Bergmann, T., Cid Fernandes, R., Winge, C., & Schmitt, H. 2006, MNRAS, 371, 170.
Barbosa, F. K., Storchi-Bergmann, McGregor, P., Vale, T. B., Riffel, R. A.., 2014, MNRAS, 455, 2353.
Bigiel, F., Leroy, A., Walter, F., Brinks, E., de Blok, W. J. G., Madore, B., Thornley, M. D., 2008, AJ, 136, 2846.
Bradt, H. V., Burke, B. F., Canizares, C. R., Greenfield, P. E., Kelley, R. L., McClintock, J. E., van Paradijs, J. & Koski, A. T., 1978, ApJ, 226, 111.

Brum, C., Riffel, R. A., Storchi-Bergmann, T., Robinson, A., Schnorr Müller, A., Lena, D., 2017, MNRAS, 469, 3405.
Cid Fernandes, R. et al. 2004, MNRAS, 355, 273
Colina, L. et al., 2015, A&A, 578, 48.
Dale, D. A., Sheth, K., Helou, G., Regan, M. W., & Hüttemeister, S., 2005, ApJ, 129, 2197.
Davies, R. I. et al. 2007, ApJ, 671, 1388
Davies, R. I., Maciejewski, W., Hicks, E. K. S., Tacconi, L. J., Genzel, R., Engel, H., 2009, ApJ, 702, 114.
Davies, R. I, et al., 2015, ApJ, 806, 127.
Davies, R. I, et al., 2017, MNRAS, 466, 4917.
de Vaucouleurs, G., de Vaucouleurs, A., Corwin, H. G., Jr., et al. 1991, Third Reference Catalogue of Bright Galaxies, Volume I: Explanations and references, Volume II: Data for galaxies between 0h and 12h, Volume III: Data for galaxies between 12h and 24h (New York: Springer)
Diniz, M. R., Riffel, R. A., Stochi-Bergmann, T., Winge, C., 2015, MNRAS, 453, 1727.
Dors, O. L., Storchi-Bergmann, T., Riffel, R. A., Schmidt, A. A, 2008, A&A, 482, 59.
Dors, O. L., Riffel, R. A., Cardaci, M. V., Hägele, G. F., Krabbe, A. C., Pérez-Montero, E., Rodrigues, I., 2012, MNRAS, 422, 252.
Dors, O. L., Cardaci, M., Hägele, G., Krabbe, A., 2014, MNRAS, 442, 1291.
Durré M. & Mould J., 2014, ApJ, 784, 79.
Croton D., et al., 2006, MNRAS, 365, 11
Falcoón-Barroso, J., Ramos Almeida, C., Böker, T., Schinnerer, E., Knapen, J. H., Lançon, A., Ryder, S., 2014, MNRAS, 438, 329.
Ferrarese, L., & Merritt, D., 2000, ApJ, 539, L9.
Ferrarese, L. & Ford, H. 2005, SSRv, 116, 523
Ferruit, P., Mundell, C. G., Nagar, N. M., Emsellem, E., Pécontal, E., Wilson, A. S., Schinnerer, E. 2004, MNRAS, 352, 1180.
Frank, J, King, A. & Raine, D. J., 2002, Accretion Power in Astrophysics, Cambridge Univ. Press
Ciotti, L., et al. 2010, ApJ 717, 707
Elvis, M. 2000, ApJ, 545, 63
Fabian, A. 2012, ARA&A, 50, 455
Frank, J., King, A. R., & Raine, D. J. 2002, Accretion Power in Astrophysics (3rd ed.; Cambridge: Cambridge Univ. Press)
Galliano, E., & Alloin, D. 2008, A&A, 487, 519.
Gebhardt, K., Bender, R., Bower, G., Dressler, A., Faber, S. M., Filippenko, A. V., Green, R., Grillmair, C., Ho, L. C., Kormendy, J., Lauer, T. R., Magorrian, J., Pinkney, J., Richstone, D., & Tremaine, S., 2000, ApJ, 539, L13.
González Delgado, R.M., Heckman, T. & Leitherer, C. 2001, ApJ, 546, 845.
González Delgado, R. M., Arribas, S., Pérez, E., Heckman, T., 2002, ApJ, 579, 188.
Graham, A. W., Onken, C. A., Athanassoula, E., Combes, F., 2011, MNRAS, 412, 2211.
Gu, Q., Melnick, J., Cid Fernandes, R., Kunth, D., Terlevich, E., Terlevich, R., 2006, MNRAS, 366, 480.
Heckman, T. M. & Best, P. N. 2014, ARA&A, 52, 589.
Hicks, E. K. S., Davies, R. I., Maciejewski, W., Emsellem, E., Malkan, M. A., Dumas, G., Müller-Sánchez, F., Rivers, A., 2013, ApJ, 768, 107.
Hopkins & Quataert 2010, MNRAS, 407, 1529
Hopkins, P. F. 2012, MNRAS, 420, 8.
Ichikawa, K., Ricci, C., Ueda, Y., Matsuoka, K., Toba, Y., Kawamuro, T., Trakhtenbrot, B., Koss, M. J., 2017, ApJ, 835, 74.
Kauffmann & Heckman 2009, MNRAS, 397, 135
Kennicutt, R. C., 1998, ARAA, 36, 189.
Kennicutt, R. C. et al., 2007, ApJ, 671, 333.
Kormendy, J. & Ho, L. C, 2013, ARA&A, 51, 511
Lamperti, I. et al., 2017, MNRAS, 467, 540.

Makarov, D., Prugniel, P., Terekhova, N., Courtois, H., Vauglin, I., 2014, A&A, 570, 13

Malkan, M. A., Gorjian, V. & Tam, R., 1998, ApJS, 117,25.

Martini, P., et al. 2013, MNRAS, 420, 2249

Mazzalay, X. et al., 2013, MNRAS, 428, 2389.

Mazzalay, X. et al., 2014, MNRAS, 438, 2036.

McGregor, P. J., Hart, J., Conroy, P. G., Pfitzner, M. L., Bloxham, G. J., Jones, D. J., Downing, M. D., Dawson, M., Young, P., Jarnyk, M., &Van Harmelen, J. 2003, Proceedings of the SPIE, 4841, 1581.

Mulchaey, J. S., Wilson, A. S., Bower, G. A., Heckman, T. M., Krolik, J. H., Miley, G. K., 1994, ApJ, 433, 625.

Müller-Sánchez F., Davies R. I., Eisenhauer F., Tacconi L. J., Genzel R., Sternberg A., 2006, A&A, 454, 492.

Müller-Sánchez, F., Davies, R. I., Genzel, R., Tacconi, L. J., Eisenhauer, F., Hicks, E. K. S., Friedrich, S., & Sternberg, A., 2009, ApJ, 691, 749.

Müller Sánchez, F. et al. 2011, ApJ, 739, 69

Nagar, N. M., Wilson, A. S., Mulchaey, J. S. & Gallimore, J. F., 1999, ApJS, 120, 209.

Noguchi, K., Terashima, Y., Ishino, Y., Hashimoto, Y., Koss, M., Ueda, Y., Awaki, H., 2010, ApJ, 711, 144.

Onken, C. et al., 2014, ApJ, 791, 37.

Osterbrock, D. E. & Ferland, G. J., 2006, Astrophysics of Gaseous Nebulae and Active Galactic Nuclei, Second Edition, University Science Books, Mill Valley, California.

Ramos Almeida, C. et al., 2014, MNRAS, 445, 1130.

Riffel, R. A.., Sorchi-Bergmann, T., Winge, C., Barbosa, F. K. B., 2006, MNRAS, 373, 2.

Riffel, R. A., Storchi-Bergmann, T., Winge, C., McGregor, P., Beck, T. & Schmitt, H., 2008, MNRAS, 385, 1129

Riffel, R. A., Storchi-Bergmann, T., McGregor, P., 2009, ApJ, 698, 1767

Riffel, R. A.., Storchi-Bergmann, T. & Nagar, N. M., 2010, MNRAS, 404, 166.

Riffel, R. A.. & Storchi-Bergmann, T., Riffel, R., & Pastoriza, M. G., 2010, ApJ, 713, 469.

Riffel, R. A.. & Storchi-Bergmann, T., 2011, MNRAS, 411, 469.

Riffel, R. A.. & Storchi-Bergmann, T., 2011, MNRAS, 417, 2752.

Riffel, R. A., Storchi-Bergmann, T., Winge, C., 2013, 430, 2249.

Riffel, R. A., Vale, T. B., Storchi-Bergmann, T., McGregor, P. J., 2014, MNRAS, 442, 656.

Riffel, R. A., Storchi-Bergmann, T., Riffel, R., ApJ, 2014, 780, 24.

Riffel, R. A., Storchi-Bergmann, T., Riffel, R., 2015, MNRAS, 451, 3587.

Riffel, R. A. et al. 2016, MNRAS, 461, 4192.

Riffel, R. A. et al. 2017, MNRAS, 470, 992.

Riffel, R., Rodríguez-Ardila, A. & Pastoriza, M. G., 2006, A&A, 457, 61.

Riffel, R., Pastoriza, M. G., Rodríguez-Ardila, A., Bonatto, C., 2009, MNRAS, 400, 273.

Riffel, R., Riffel, R. A.., Ferrari, F., Storchi-Bergmann, T., 2011. MNRAS, 416, 493.

Riffel, R., Rodríguez-Ardila, A., Aleman, I., Brotherton, M. S., Pastoriza, M. G., Bonatto, C., Dors, O. L., 2013, MNRAS, 430, 2002.

Rosario D. J., Whittle M., Nelson C. H. & Wilson A. S., 2010, MNRAS, 408, 565.

Schmidt, M., 1959, ApJ, 129, 243.

Schmitt, H. R., Ulvestad, J. S., Antonucci, R. R. J., Kinney, A. L., 2001, ApJS, 132, 199.

Schmitt, H. R., Donley, J. L., Antonucci, R. R. J., Hutchings, J. B., Kinney, A. L., 2003, ApJS, 148, 327.

Scoville, N. Z., Hall, D. N. B., Kleinmann, S. G., & Ridgway, S. T. 1982, 253, 136.

Shankar, F. et al. 2009, ApJ, 690, 20

Sakamoto, K.et al. 2010, ApJ, 725, L228

Schnorr-Müller A., Storchi-Bergmann T., Nagar N. M., Robinson A., Lena D., Riffel R. A. & Couto G. S., 2014, MNRAS, 437, 1708,

Schonel, A. J., Riffel, R. A., Stochi-Bergmann, T., Winge, C., 2014, MNRAS, 445, 414.

Schonel, A. J., Riffel, R. A., Stochi-Bergmann, T., Riffel, R., 2017, MNRAS, 464, 1771.

Simoes Lopes et al. 2007, ApJ, 655, 718

Shi, L., Gu, Q. S., & Peng, Z. X. 2006, A&A, 450, 15.

Skrutskie, M., F. et al., 2006, AJ, 131, 1163.

Somerville et al. 2008, MNRAS, 391, 481

Springel et al. 2005, MNRAS, 361, 776

Storchi-Bergmann, T., Winge, C., Ward, M. & Wilson, A. S., 1999, MNRAS, 304, 35.

Storchi-Bergmann et al. 2000, ApJ, 544, 747.

Storchi-Bergmann et al. 2001, ApJ, 559, 147

Storchi-Bergmann, T., McGregor, P. J., Riffel, R. A., Simões Lopes, R., Beck, T., Dopita, M., 2009, MNRAS, 394, 1148.

Storchi-Bergmann, T., Simões Lopes, R., McGregor, P. Riffel, R. A.., Beck, T., Martini, P., 2010, MNRAS, 402, 819.

Storchi-Bergmann, T., Riffel, R. A.., Riffel, R., Diniz, M. R., Borges Vale, T., McGregor, P. J., 2012, ApJ, 755, 87.

Terlevich E. et al. 1990, MNRAS, 242, 271.

Tremaine, S., Gebhardt, K., Bender, R., Bower, G., Dressler, A., Faber, S. M., Filippenko, A. V., Green, R., Grillmair, C., Ho, L. C., Kormendy, J., Lauer, T. R., Magorrian, J., Pinkney, J., & Richstone, D., 2002, ApJ, 574, 740.

Ulvestad J. S. & Wilson A. S., 1983, ApJl, 264, L7.

Veilleux, S. et al. 2013, ApJ, 776, 27

Zhu, G., Zaw, I., Blanton, M. R., Greenhill, L. J., 2011, ApJ, 742, 73.

Weaver, K. A., Mushotzky, R. F., Serlemitsos, P. J., Wilson, A. S., Elvis, M. & Briel, U., 1995, ApJ, 442, 597.

Whittle, M. 1992, ApJS, 79,49

Wold, M., Galliano, E., 2006, MNRAS, 369, 47.

This paper has been typeset from a TeX/LaTeX file prepared by the author.